ELSEVIER

Contents lists available at ScienceDirect

Minerals Engineering

journal homepage: www.elsevier.com/locate/mineng



Water droplets and air bubbles at magnesite nano-rough surfaces: Analysis of induction time, adhesion and detachment using a dynamic microbalance



Zhanglei Zhu^{a,b}, Donghui Wang^{a,b}, Bin Yang^a, Wanzhong Yin^{a,c,*}, Jaroslaw W. Drelich^{b,*}

- a School of Resources and Civil Engineering, Northeastern University, Shenyang 110819, China
- b Department of Materials Science and Engineering, Michigan Technological University, Houghton 49931, United States
- ^c Genetic Mineral Processing Research Center, Northeastern University, Shenyang 110819, China

ARTICLE INFO

Keywords: Magnesite Surface roughness Contact angle, wettability Adhesion force

ABSTRACT

Surface roughness affects the interactions of solids with droplets and bubbles. In this study, natural magnesite lumps were polished by a series of sandpapers and diamond to produce four magnesite specimens having 2 to 240 nm root-mean-square roughness. The dynamic measurements of attachment, spreading, adhesion, and separation with a high-sensitivity microelectronic mechanical balance revealed the effect of surface nano-scaled roughness on the induction time and forces of spreading, adhesion and separation for both water droplets and air bubbles. It was found that the increasing nano-scaled roughness enhances the spreading of water on hydrophilic magnesite and strengthens the water-magnesite adhesive contact. Nano-roughness also causes delays in attachment of air bubbles to magnesite surface, inhibits displacement of water by adhering air bubbles, and reduces the adhesive strength of air bubbles to the magnesite surface, factors that might slow down the flotation separation.

1. Introduction

Flotation is a complex physicochemical process involving at least three phases (solid, liquid and gas), and was invented to selectively separate targeted particles from other particles suspended in the pulp (Crabtree and Vincent, 1962). Selectivity of flotation separation is driven by differences in particle natural or induced hydrophobicity, combined with a control over the particle–particle and particle-bubble colloidal interactions (Chau et al., 2009; Drelich and Marmur, 2018). Although the process may appear relatively simple, there are up to 100 variables that can impact the flotation process (Shean and Cilliers, 2011).

The effect of surface roughness on flotation of mineral particles has been in focus among several research laboratories in the last two decades, but the published reports often lead to contradicting conclusions, as already reviewed in the previous paper (Guven et al., 2015). For example, Ulusoy and Yekeler (2005) reported that the increased surface roughness leads to a reduced water contact angle and floatability of quartz, talc, barite, and calcite particles. In another study, Hicyilmaz et al. (2005) reported enhanced floatability of barite particles with smoother surfaces in the presence of A-845 (Cytec) succinamate surfactant; autogenous milling was used to lower both barite particle

roughness and acuteness. Ahmed (2010), on the other hand, found that particles with rough surfaces, containing a larger number of microstructural defects, stabilize the froth, and improve the flotation kinetics. Guven et al. (2015) studied the influence of particle roughness on flotation of methylated glass beads and demonstrated that particle surface roughness benefits the flotation recovery. Later, Hassas et al. (2016) confirmed this finding for glass beads but using hexadecyl trimethyl ammonium bromide as a collector. Li et al. (2019) also demonstrated the facilitating effect of micro-sized surface roughness on the floatability of malachite particles. The effect of surface roughness on the bubble-particle induction time was also analyzed. Chen et al. (2018), Xia (2017) measured the attachment time for air bubbles in contact with natural coal particles. The authors reported that as surface roughness increases, the attachment time increases and at the same time, the bubble-coal adhesion contact area decreases. Xing et al. (2019) additionally reported that hypobaric treatment can mitigate the adverse effects of surface roughness on attachment time.

Although the effects of particle surface roughness on flotation and bubble-particle attachment are reported in the literature quite well, understanding the factors that drive these effects appears incomplete yet. In AFM colloidal force measurements, Karakas and Hassas (2016) demonstrated higher repulsions between smooth particles as compared

E-mail addresses: yinwanzhong@mail.neu.edu.cn (W. Yin), jwdrelic@mtu.edu (J.W. Drelich).

^{*} Corresponding authors at: Department of Materials Science and Engineering, Michigan Technological University, Houghton 49931, United States (J.W. Drelich) and School of Resources and Civil Engineering, Northeastern University, Shenyang 110819, China (W. Yin).

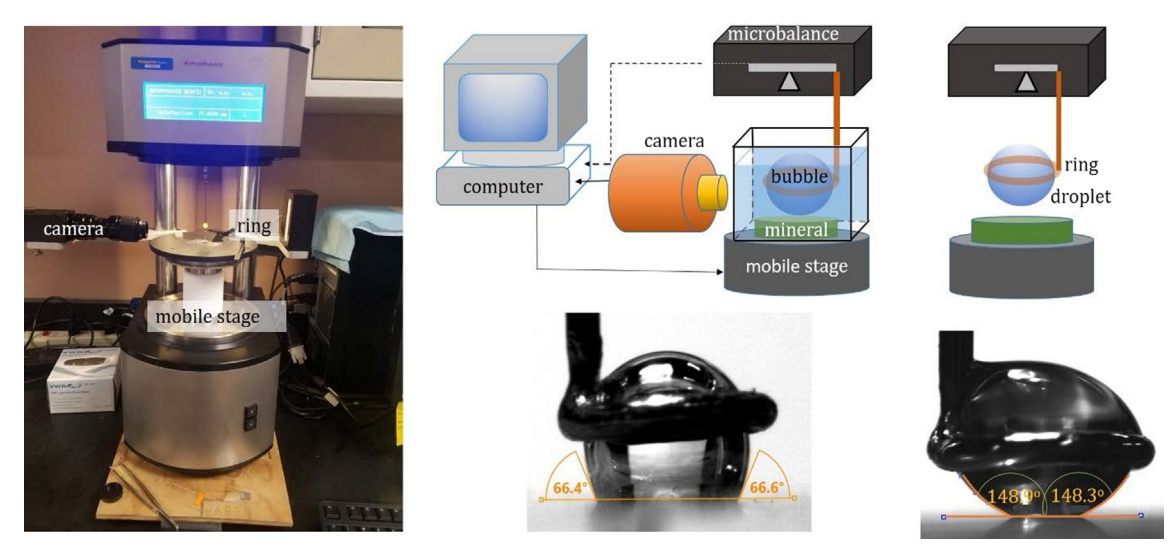


Fig. 1. Experimental system used in this study.

to rough particles. Feng and Aldrich (2000) reported that the rough surfaces with a high concentration of microstructural defects provided more active centers for accelerated dissolution of particles, benefiting the adsorption of reagents onto the particle surfaces, and leading to enhance flotation performance. Theoretical modeling revealed that nano-scaled asperities can reduce energy barriers in interactions between rough particles and gas bubbles (Drelich, 2018; Drelich and Bowen, 2015). Micro-scaled roughness, on the other hand, does not have the same effect, and it can stabilize a water film, particularly for hydrophilic substrates with the water contact angle is less than 65–70° (Drelich et al., 2011).

Previously, we demonstrated the positive effect of particle nanoscaled roughness on flotation recovery of magnesite (Zhu et al., 2020). We also speculated through theoretical modeling that nano-scale asperities lower energy barriers during particle-bubble interactions. In this study, we examine directly the effect of nano-scaled magnesite surface roughness on the attachment, spreading, adhesion and separation of both the water droplets and air bubbles to understand whether there are other factors than energy barriers that could be accounted to flotation performance of rough particles. The measurements were carried out using the high-sensitivity microelectronic mechanical balance equipped with a camera and data acquisition software, which can instantly record the adhesion force and image a shape of the droplet/ bubble, from which both contact angles and dimensions are extracted. The results reveal that with increasing surface nano-scaled roughness, the adhesion of water increases, delaying attachment of air bubble and decreasing bubble adhesion.

2. Experimental

2.1. Mineral samples

High quality magnesite lumps were selected from an ore mined in Dandong, Liaoning Province, China. The x-ray fluorescence analysis confirmed a high purity of specimens with more than 97 wt.% MgCO $_3$. The magnesite lumps were cut into approx. $10\times10\times5$ mm specimens using a metallographic saw. The grinding and polishing of surfaces were carried out by abrasive sandpaper of 120, 400, and 1200 mesh and 1 μm diamond powder. The polished magnesite samples were washed with ethanol and deionized water several times and then dried before adhesion force measurements.

2.2. Surface roughness measurement

In this study, $10 \times 10 \ \mu m$ AFM (atomic force microscopy) images of magnesite surfaces were collected with an MFP-3D Origin ⁺ AFM instrument (Oxford Corporation, United States) using the AC Air Topography mode. Three to five different locations on the magnesite specimen surface were randomly selected and imaged. The reported roughness values include root-mean-square roughness (R_q), arithmetic roughness (R_a), surface area ratio (R_{SA}), skewness (R_{sk}), and kurtosis (R_{kn}) defined as follows:

$$R_q = \sqrt{\frac{1}{N} \sum_{i=1}^{N} Z_i^2} \tag{1}$$

$$R_a = \frac{1}{N} \sum_{i=1}^{N} |Z_i - \bar{Z}| \tag{2}$$

$$R_{SA} = \frac{S_a}{S_p} \tag{3}$$

$$R_{sk} = \frac{1}{N} \sum_{i=1}^{N} \left(\frac{Z_i - \bar{Z}}{\sigma} \right)^3 \tag{4}$$

$$R_{ku} = \frac{1}{N} \sum_{i=1}^{N} \left(\frac{Z_i - \bar{Z}}{\sigma} \right)^4 - 3 \tag{5}$$

where $\sigma = \sqrt{\frac{1}{N-1}\sum_{i=1}^{N}(Z_i-\bar{Z})^2}$, Z_i is the height at a given pixel i, N is the total number of pixels in the image, and \bar{Z} is the average height of the entire image. S_a and S_p refer to the actual and projected surface area, respectively. The reported are the calculated average and standard deviation values.

2.3. Adhesion force and contact angle measurements

A high-sensitivity microelectronic mechanical balance, called Dynamic Contact Angle Meter and Tensiometer instrument by the manufacturer (DCAT 21, Dataphysics, Germany), equipped with a CCD camera was used in this study to record adhesion forces between water droplet and air bubble and magnesite samples (Fig. 1). Fig. 2 presents examples of typical recordings for water droplet/magnesite and air bubble/magnesite systems. About 4 μ L-volume water droplet or gas bubble was suspended with a micro-syringe on a ring (internal and external diameter of 2.06 mm and 2.42 mm, respectively) connected to a microbalance and the initial balance force was set to zero (point A in Fig. 2). The force versus distance loop comprised five distinctive steps (Fig. 2): i) the sample was approached to either water droplet or gas bubble without any recordable interactions (from point A to B), ii)

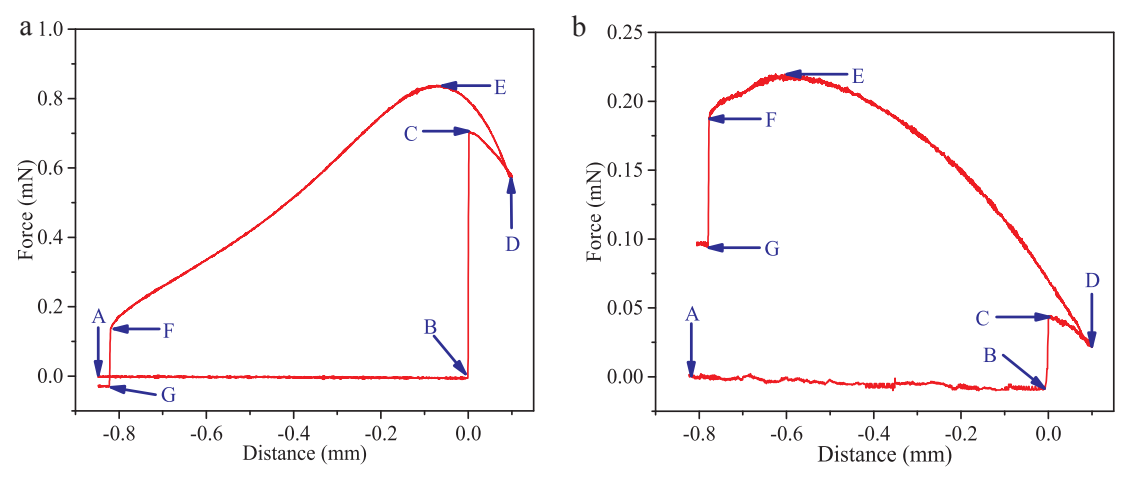


Fig. 2. A typical force curves for: a) water droplet, and b) air bubble in interactions with magnesite surface.

process of attachment between water droplet/gas bubble and mineral surface causing spreading (point C), iii) mechanical compression of attached phases (from point C to D), iv) stretching of droplet/bubble (from point D to E), and v) separation of ring-hosted droplet/bubble from the mineral surface (point F). The moving speed of mobile stage with mineral sample was 0.03 mm/s and 0.01 mm/s before and after attachment processes, respectively.

The sample was lifted upward toward the droplet (or bubble) by a programmed motor movement until the microbalance detected the suspended droplet (or bubble) (point B). Because of a continuing submersion of air bubble into water (from point A to B), a small negative force caused by hydrostatic pressure was recorded before the bubble attached to the mineral surface.

An attractive force was measured at point C, which reflects the force for the droplet (bubble) to spread spontaneously on the mineral surface after attachment. The attachment of water droplet to the mineral specimen was instantaneous whereas it was delayed for air bubble and delay increased with increasing mineral surface roughness. The time of delay is called *induction time* in this contribution.

The force curve section from point C to D represents the compression of droplet (bubble) against the mineral surface. The compression distance was set at 0.1 mm in this study, and was used to secure enlarged contact area between droplet (bubble) and mineral surface, useful for reproducible adhesion force measurements.

At point D, the movement of stage with the mineral sample was reversed, causing the water droplet (air bubble) to be stretched and its base diameter to reduce. The maximum value at point E in the force curve represents the maximum adhesion force. The continuation of stretching beyond point F concludes with separation of droplet (bubble) from the mineral surface at critical point F, at which pull-off force is recorded.

The entire process of attachment, spreading, compression, stretching, and separation was continuously recorded with the CCD camera, having a resolution of 0.133 s. From recorded images, the droplet (bubble) dimensions, shapes and contact angles were determined (Fig. 1). All the experimental values of contact angles, base diameter and forces reported in this study are the average of at least four reproducible tests. All measurements in this study were carried out at a room temperature of about 22 °C.

3. Results and discussion

3.1. Surface roughness

Fig. 3 shows the representative 3-dimensional (3D) AFM images of $10.0\times10.0~\mu m^2$ magnesite surfaces after grinding and polishing. The

3D AFM images confirmed a reduction in surface roughness of mineral surface after each step of polishing using the sandpaper with increasing mesh number and then using a fine diamond powder. The average values for surface roughness parameters (R_q and R_a) and surface area ratio (R_{SA}), together with their standard deviation values, are listed in Table 1.

The R_q and R_a roughness values for magnesite surface decreased from 240 \pm 26 nm and 202 \pm 14 nm, respectively, for mineral polished with 120 mesh sandpaper to 42 \pm 8 nm and 31 \pm 7 nm, respectively, after final polishing with sandpaper having 1200 mesh (Table 1). At the same steps of polishing with sandpaper of increasing mesh, the surface area ratio for magnesite surface decreased from 1.113 \pm 0.034 to 1.011 \pm 0.002. Final polishing of magnesite with 1 μm diamond powder made the surface smooth with $R_q=2.3\,\pm\,0.2$ nm, $R_a=1.8\,\pm\,0.1$ nm and $R_{SA}=1.006\,\pm\,0.001$. It should be noticed that R_{SA} values determined through AFM roughness analysis are typically underestimated because the cantilever tip cannot image surface features that are smaller than the tip dimension, and due to a tip deconvolution effects (Lai and Irene, 1999; Ramon-Torregrosa et al., 2008).

Both skewness (R_{sk}) and kurtosis (R_{ku}) values for polished magnesite samples were close to zero (Table 1), suggesting that polishing of magnesite produced nano-rough surfaces with spatial distribution of asperity variations that is symmetrical and follows a normal distribution. Low values for R_{ku} indicate on uniformity of asperity variation for all samples polished with sandpapers. After final polishing with 1 μ m diamond powder, both R_{sk} and R_{ku} values were elevated indicating that some non-uniform scratches produced by sandpaper were most likely left on the surface.

3.2. Water droplet on magnesite surface

Fig. 4 shows sequences of images during water droplet interactions with magnesite samples of varying nano-roughness at key points of force curve (A through G; Fig. 2) including: i) sample approaching the water droplet (A), ii) water droplet attachment to the sample (B), iii) spontaneous spreading of the water droplet (C), iv) droplet compression (D), followed by v) stretching (E), and the final vi) split of the droplet (F). For all four samples, the droplet attachment and spreading events took place spontaneously, soon after the first contact of droplet with mineral, within 0.133 s, and could be captured on one CCD camera frame only (Table 2); therefore, no water droplet spreading kinetics could be analyzed in detail. Stretching the water droplet led to a critical diameter of ring-magnesite water bridge that ruptured before separation of entire droplet from the magnesite sample. A large adhesion force prevented detachment of water from the mineral surface. As shown in

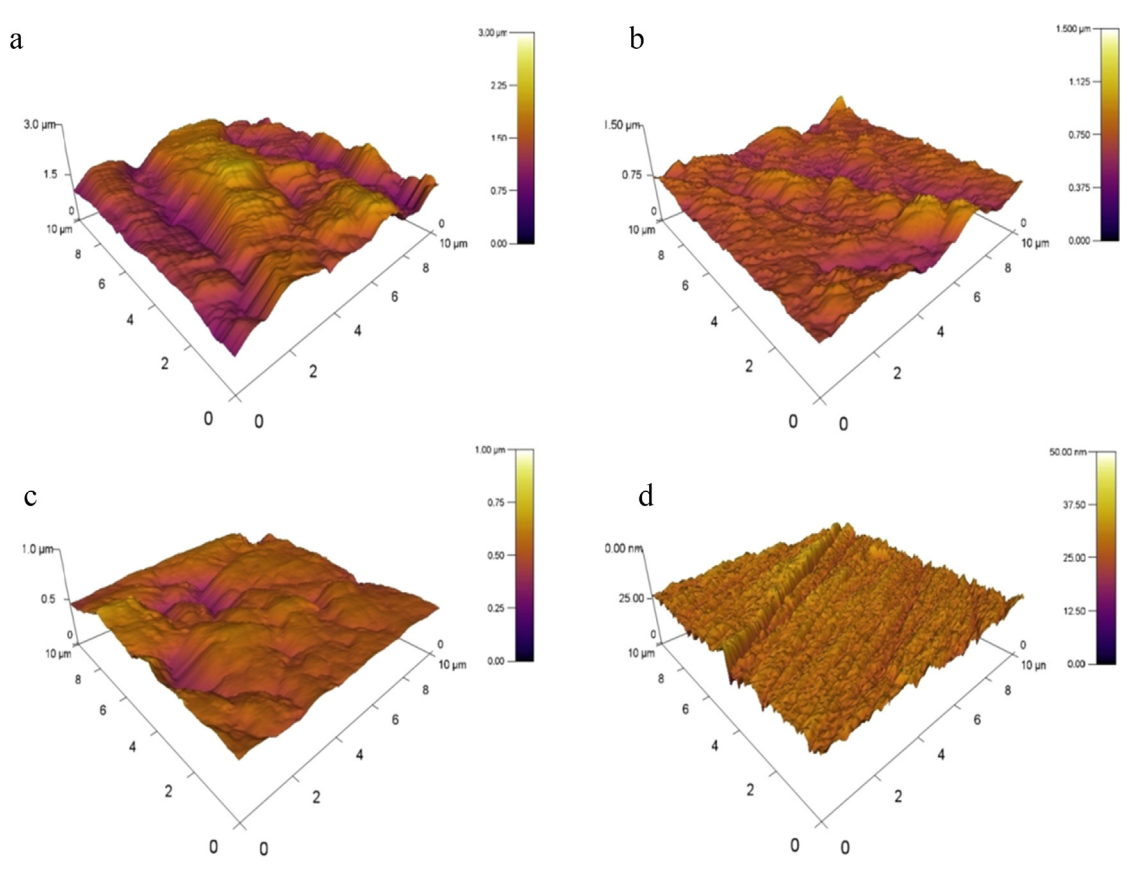


Fig. 3. Examples of 3D AFM images of magnesite surfaces after polishing with: a) 120 mesh sandpaper; b) 400 mesh sandpaper; c) 1200 mesh sandpaper; and d) 1 μ m diamond.

column F of Fig. 4, the shape of capillary water bridge formed was influenced by the water contact angle at the mineral surface (base of the water bridge). Because the contact angle decreased with increasing $R_{\rm q}$ value (as will be shown later), the separation time, which included time to form unstable capillary bridge, increased with increasing $R_{\rm q}$ value (Table 2).

After rupturing, a portion of water droplet remained in the holding ring and rest remained on the magnesite surface in shape of a lens. The shape of the water lens remaining on the magnesite surface was affected by surface roughness. The lens diameter increased with increasing roughness of the magnesite surface at the expense of its height, clearly indicating on decreasing water contact angle.

Fig. 5 summarizes the force and contact angle values measured during each sequence of water droplet spreading, stretching and pull-off using the magnesite samples of different nano-roughness characteristics, plotted as a function of RMS roughness (R_q). The force values are presented as both raw (F) and normalized data (force per contact perimeter = $F/\pi d$, where d is the droplet base diameter).

There are three different sets of force and contact angle values, similar to what was reported and discussed in details in our previous contributions (Drelich, 2019; Jiang et al., 2018; Sun et al., 2018a, b; Sun et al., 2020; Wang et al., 2020). The force measured at point C of the force curve represents the *spreading force*, and the contact angle

measured at this point refers to advancing (water) contact angle (see Fig. 2 for identification of key points on the force curves). At point E, the maximum adhesion force is measured and the contact angle measured is called most stable contact angle. Finally, at point F, the pull-off force is typically measured, with the contact angle that represents the receding (water) contact angles. Because water-magnesite adhesion forces exceeded water cohesion forces in these experiments, the water droplet split for two portions before it was separated (pull-off) entirely from the mineral surface. This means that the pull-off force measured in these experiments does not represent the force necessary to separate water from mineral surface. Also the contact angle value measured at point F is likely higher than the receding contact angle value that could be measured during a complete separation of two phases. For that reason, the interpretation and meaning of data captured at point F and presented in Fig. 5 are limited here.

As shown in Fig. 5, the forces increase with increasing roughness. The spreading, maximum adhesion, and pull-off forces (and their normalized values) increase from 0.5 mN (59 mN/m) to 0.6 mN (63 mN/m), 0.7 mN (79 mN/m) to 0.8 mN (85 mN/m), and 0.10 mN (13.0 mN/m) to 0.14 mN (13.5 mN/m), respectively, when the $R_{\rm q}$ increases from 2 nm to 240 nm. The normalized force values are only slightly affected by roughness suggesting that the three-phase contact line length is one of key parameters in interpretation of experimental force values. The

Table 1Surface roughness parameters for magnesite surfaces after four stages of polishing.

-0.2 ± 0.6
0.2 ± 0.6
1.4 ± 1.7
11 ± 15

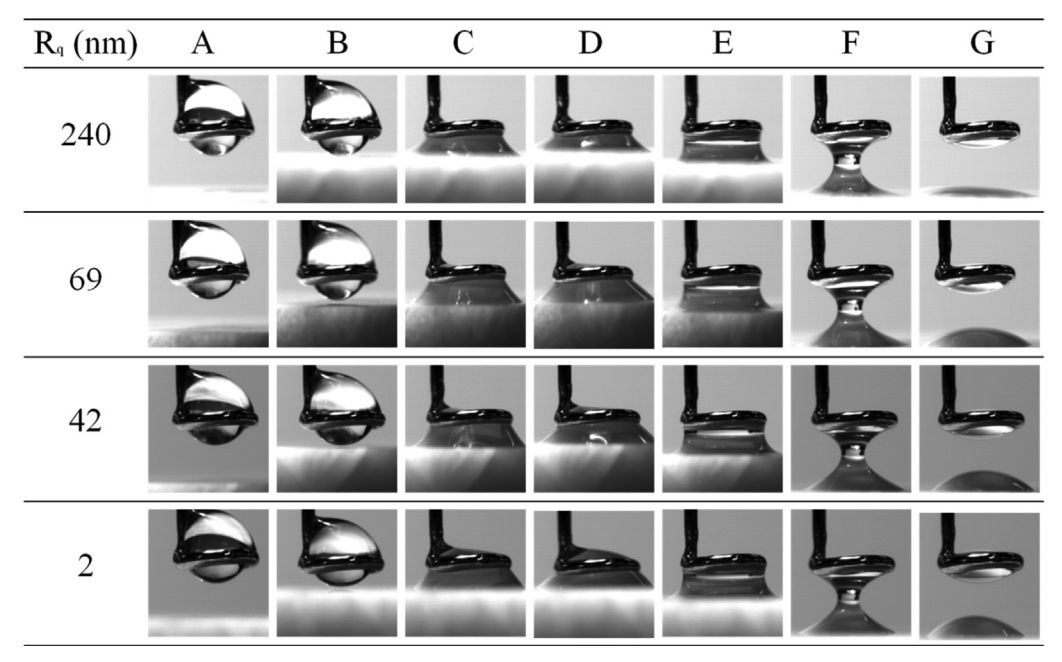


Fig. 4. Images of water droplets during interactions with magnesite surface of different roughness.

Table 2Interaction time between water droplet/air bubble and magnesite surfaces with varying surface roughness.

R _q (nm)	Induction time (s)		Spreading time (s)		Separation time (s)	
	Droplet	Bubble	Droplet	Bubble	Droplet	Bubble
240 ± 26	≤0.13	12.0	≤0.13	0.40	89	0.53
69 ± 12 42 ± 8	≤ 0.13 ≤ 0.13	8.0 5.3	≤ 0.13 ≤ 0.13	0.40 ≤ 0.13	87 80	1.6 7.1
2.3 ± 0.2	≤0.13	\leq 0.13	≤0.13	≤0.13	75	8.1

experimental forces consist of two components (6) (Chen et al., 2016; Qian and Gao, 2006): i) one is the vertical component of liquid–gas interfacial tension acting along the perimeter of triple contact line, known as surface tension force (F_T) , ii) the other is the Laplace pressure force (F_L) which is induced by the pressure difference across the liquid–gas interface for a stretched droplet:

$$F = F_T - F_L = l\gamma \sin\theta - A\Delta P \tag{6}$$

where l is the droplet base perimeter, A is the droplet base projected contact area ($A=\pi r^2$ for a circle), γ is the liquid–gas interfacial tension, θ is the contact angle, ΔP is the Laplace pressure defined as $\Delta P = \gamma(\frac{1}{D} + \frac{1}{R})$ where D and R are the principal radii of the water–air interface.

The three-phase contact line perimeter for a droplet on a smooth, homogeneous and flat solid surface becomes circular and equal to $l=2\pi r$ (r is the radius of droplet base). For rough hydrophilic surface $l>2\pi r$, whereas it is $l<2\pi r$ for rough hydrophobic surface. A random roughness of hydrophilic solid, such as magnesite in this study, reinforces a contortion of the water droplet line in both vertical and lateral directions, both of which are difficult to quantify experimentally and theoretically. It is however, safe to conclude that the increase in the contact line length (l) is the primary cause of increasing the surface tension force component in Eq. (6), without any major effect on the capillary pressure force component, and on total adhesion force, in agreement with data in Fig. 5.

Eq. (6) also indicates that the adhesion force measured for water droplets on roughened magnesite surface is affected by contact angle. As shown in Fig. 5c, the advancing, most stable, and "receding" contact angles decrease from 51 \pm 2° to 21 \pm 2°, 28 \pm 2° to 20 \pm 2°, and

 $24 \pm 2^{\circ}$ to $8 \pm 1^{\circ}$, respectively, when R_q increases from 2 nm to 240 nm. The effect of surface roughness on contact angle is predicted by the Wenzel equation (Wenzel, 1936):

$$\cos\theta_{\rm W} = R_{SA} \cdot \cos\theta \tag{7}$$

where θ and θ_W are equilibrium contact angle on a smooth and rough, respectively, (and flat) solid surface; R_{SA} is the "real to projected surface area ratio." It should be recognized that in modern literature the roughness factor represents changes in the contact line on a rough surface compared to the changes in the contact line on a smooth and flat surface. Unfortunately, measurements of the contact line length and its contortion are beyond experimental capabilities in our laboratory at present. Therefore, we use original approach as proposed by Wenzel with understanding that it can provide only a rough estimate of contact angles on rough surfaces.

This Wenzel equation predicts a decrease in contact angle value for water droplet on any hydrophilic surface, when surface is roughened ($R_{SA} > 1$); in a qualitative agreement with the data in Fig. 5c. Justification of Eq. (7) can only be pursued with the most stable contact angle values, which are close to the "equilibrium" contact angles defined by the Wenzel equation. So if experimental (average) AFM R_{SA} data from Table 1 are used to calculate the contact angle (θ_s) on a smooth magnesite surface, the values are: 32 \pm 4° for R_q at 240 nm, 25 \pm 2° for R_q at 69 nm, 27 \pm 1° for R_q at 42 nm, and 28 \pm 1° for R_q at 2 nm (Table 3). A spread in contact angle is only about 7°, providing a reasonable support here for the Wenzel model, when applied to hydrophilic magnesite with nano-scaled roughness.

3.3. Air bubble on magnesite surface

Fig. 6 shows sequences of images of air bubble during its attachment, spreading and separation from magnesite samples having varying nano-roughness. There are two important differences in these sequences as compared to what was presented for water droplets in the previous section. First, attachment of air bubble to magnesite was not spontaneous. The bubble attachment to smoothest surface $(R_q=2\ \text{nm})$ was recorded on one frame (0.133 s), indicating that the induction time for the air bubble was $\leq 0.133\ \text{s}$. However, the induction time increased to 5.3 s (41 frames) for the magnesite surface with $R_q=42\ \text{nm}$, 8.0 s (60 frames) for $R_q=69\ \text{nm}$, and 12.0 s (90 frames) for

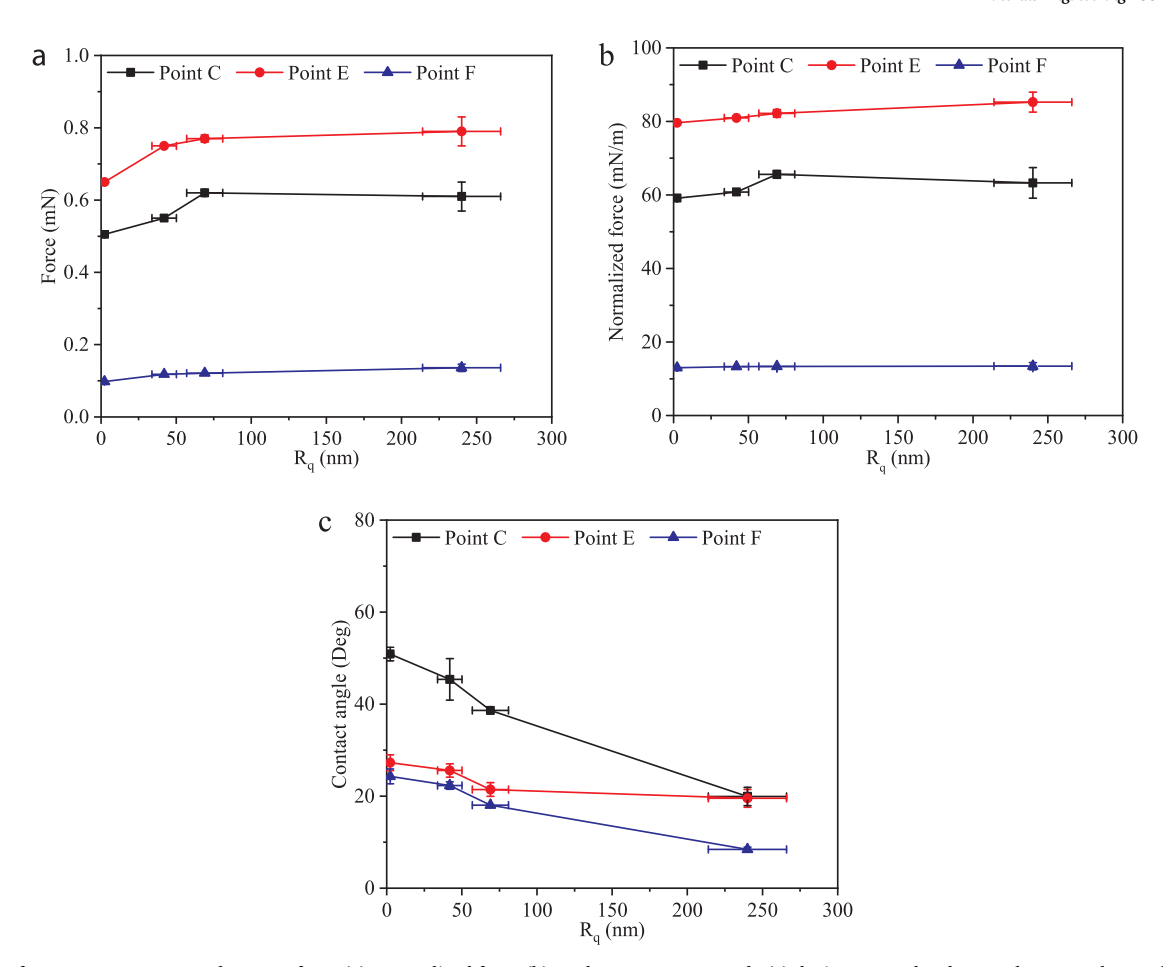


Fig. 5. Effect of root mean square roughness on force (a), normalized force (b), and water contact angle (c) during water droplet attachment and spreading (point C), at a maximum adhesion point (point E), and at a pull-off point (point F).

Table 3The calculated contact angle on a smooth magnesite surface.

R _{SA}	θ_W (deg)	θ_{S} (deg)
1.113 ± 0.034 1.031 ± 0.012 1.011 ± 0.002 1.006 ± 0.001	20 ± 2 21 ± 2 26 ± 1 28 ± 2	32 ± 4 25 ± 2 27 ± 1 28 ± 1

 $R_{\rm q}=240~\rm nm$ (Table 2). The recorded delay in attachment of air bubble clearly indicates on increasing stability of water film on magnesite surface with increasing surface nano-roughness. In relation to flotation, the data indicates on a possible delay in attachment of mineral particles to air bubbles. However, it should be recognized that the induction times recorded for air bubbles with macroscopic specimens are typically at least one-to-two orders of magnitude longer than induction times recorded for sub-millimeter particles typically floated during flotation tests (Drelich and Miller, 2012). Therefore, this effect might be of a negligible significance to flotation kinetics of fine particles. Further study is needed to quantify a correlation between induction times measured for macroscopic specimens and sub-millimeter sized particles.

Second, detachment of air bubble from magnesite was relatively easy as compare to detachment of water droplet. Entire bubble could be detached from mineral surface whereas only portion of water was removed during detachment of water droplet (see Section 3.2). Also time between maximum adhesion (E) and pull-off (F) points was shorter. From a few to several frames were recorded when the bubble was stretched beyond the point of maximum adhesion force, and the

separation time, as defined between points E and F, decreased with increasing R_q value (Table 2, separation time). Therefore, an adhesive contact between air bubble and magnesite surface appears more vulnerable to separation for nano-rough surfaces. However, it has very little, if any, effect on instability of gas bubble – magnesite particle aggregates. Detachment of a mineral particle from attached air bubble would only be possible when receding (water) contact angle established during bubble attachment (at point C in Fig. 2b) changes to advancing (water) contact angle (characteristic to point F; Fig. 2b). Such a transition is against the adhesion forces (between points C and E) that can only be overcome by deformation of gas bubble surface due to either gravity effects (associated with big particles, which elongate air bubble) or unusually strong hydrodynamic effects that increase shear stresses locally, in the area of particle-bubble contact.

Fig. 7 shows force, normalized force and water contact angle values as a function of magnesite surface roughness. As shown in Fig. 7a – b, all three forces including spreading force (point C), maximum adhesion force (point E) and pull-off force (point F) decreased with increasing roughness. For example, the normalized spreading force decreased from about 50 mN/m for $R_q=2\,\text{nm}$ to 37 mN/m for $R_q=42\,\text{nm}$ to 36 mN/m for $R_q=69\,\text{nm}$ and to 28 mN/m for $R_q=240\,\text{nm}$. The normalized maximum adhesion force decreased from about 97 mN/m for $R_q=2\,\text{nm}$ to 75 mN/m for $R_q=42\,\text{nm}$ to 66 mN/m for $R_q=69\,\text{nm}$ and to 46 mN/m for $R_q=240\,\text{nm}$. The normalized pull-off force decreased from about 130 mN/m for $R_q=2\,\text{nm}$ to 65 mN/m for $R_q=42\,\text{nm}$ to 59 mN/m for $R_q=69\,\text{nm}$ and to 32 mN/m for $R_q=42\,\text{nm}$. This is expected since the adhesion interactions between water and hydrophilic magnesite surface are enhanced by surface roughening (see previous section).

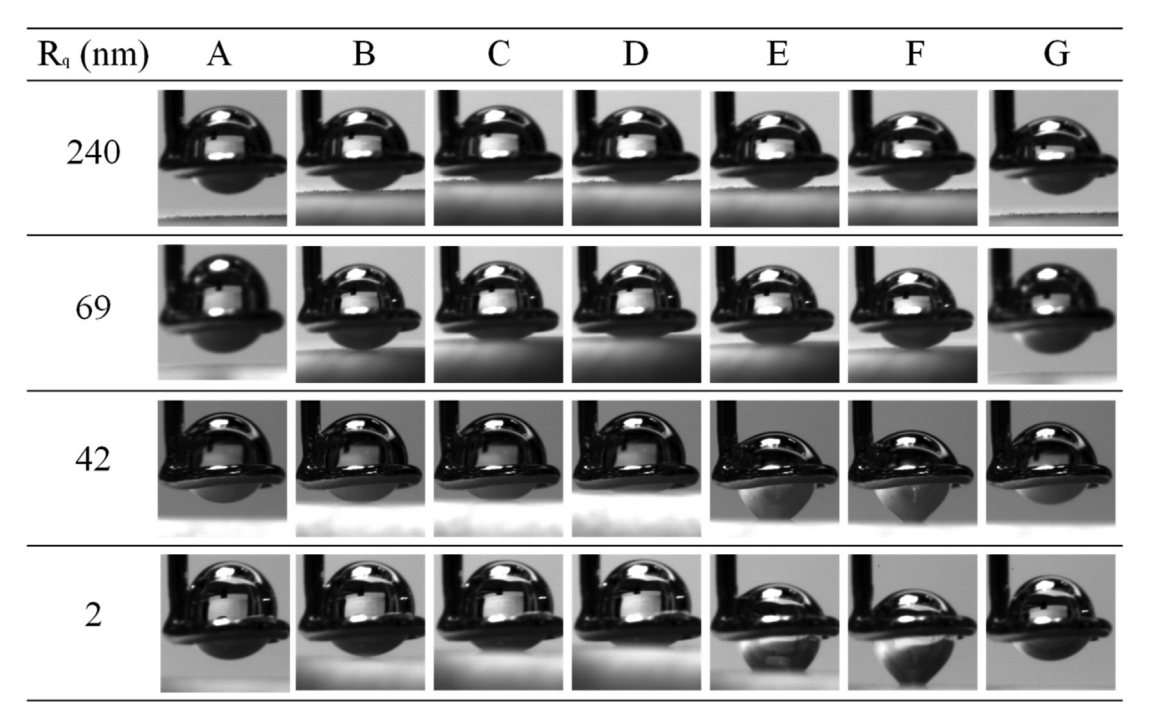


Fig. 6. Images of air bubbles in water during interactions with magnesite surface of different roughness.

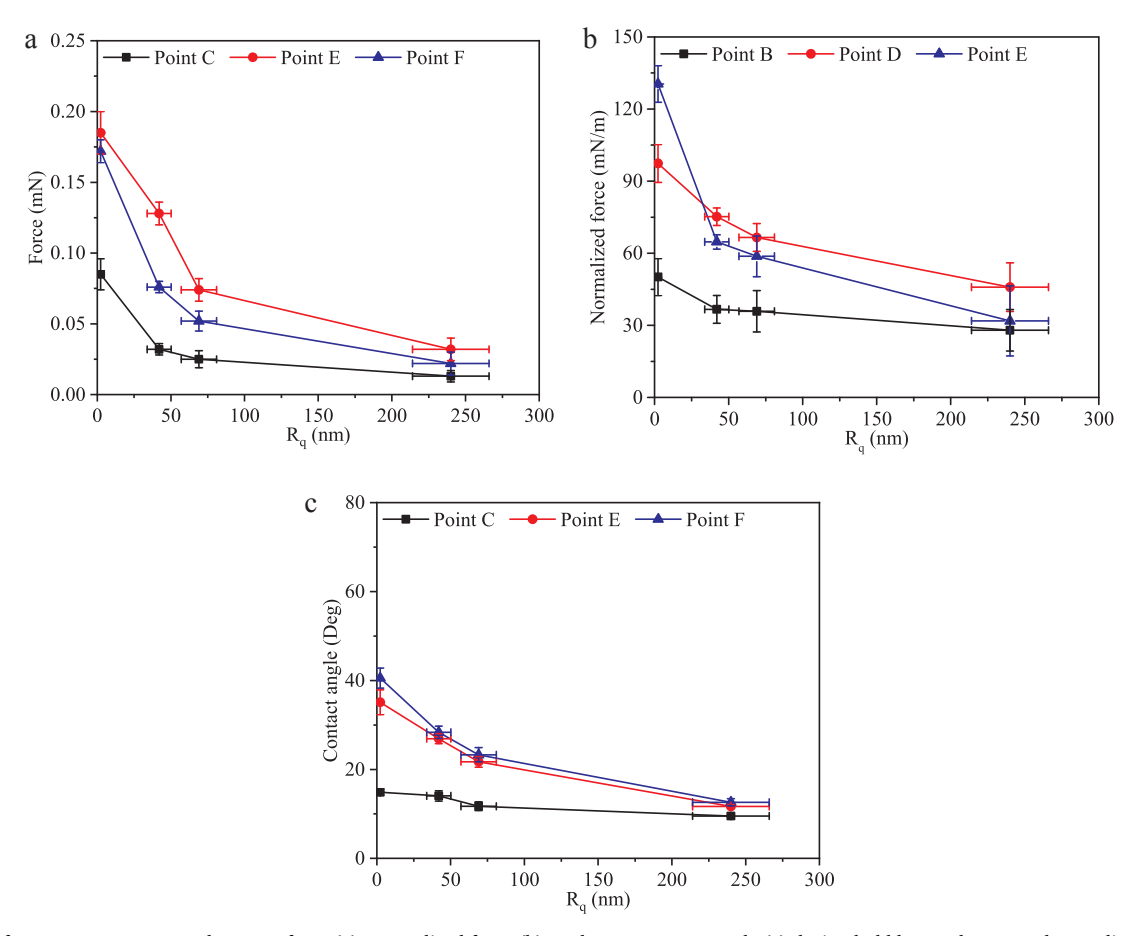


Fig. 7. Effect of root mean square roughness on force (a), normalized force (b), and water contact angle (c) during bubble attachment and spreading (point C), at a maximum adhesion point (point E), and during the bubble separation form the magnesite surface (point F).

As shown in Fig. 7c, the contact angles measured across water decreased as well. In agreement with measurements involving water droplets. The receding contact angle (measured at point C) decreased from about 15° for $R_q=2$ nm to 14° for $R_q=42$ nm to 12° for $R_q=69$ nm and less than 10° for $R_q=240$ nm. The most stable contact angle (measured at point E) decreased from about 35° for $R_q=2$ nm to 27° for $R_q=42$ nm to 22° for $R_q=69$ nm and less than 12° for $R_q=240$ nm. The advancing contact angle (measured at point F) decreased from about 41° for $R_q=2$ nm to 29° for $R_q=42$ nm to 24° for $R_q=69$ nm and less than 13° for $R_q=240$ nm.

In summary, the force and contact angle measurements provide a solid evidence that nano-scaled roughness of magnesite weakens adhesive interactions of mineral with air bubbles. Since the measurements were carried out on large specimens, it remains to be seen whether the weakening of adhesion has any consequences in flotation recovery and kinetics, and under what hydrodynamic conditions. Conceptually, weakening bubble-mineral adhesive strength might increase probability of early detachment of mineral particles from gas bubble under intense hydrodynamic conditions, typically observed in mechanical flotation cells.

4. Conclusions

The direct measurements of attachment, spreading, adhesion, and separation for water droplets and air bubbles in contact with magnesite surfaces support the followings conclusions:

- Magnesite mineral is hydrophilic, showing a preferential affinity of this mineral to water rather than to air, with the most stable (water) contact angle of 25–32 degree as determined experimentally and calculated based on the Wenzel equation.
- Nano-scaled roughness of magnesite surface enhances adhesive strength with water, which becomes more resistant to replacement with the air bubble during attachment and spreading.
- 3) Induction time for the air bubble to attach to magnesite surface increased from ≤ 0.133 s for a smooth surface to 5.3, 8.0 and 12.0 s for surfaces with root-mean-square roughness of 42, 69 and 240 nm, respectively. It suggests an opposite effect of nano-roughness on air bubble attachment as compared to the effect of bubble-mineral energy barrier that is reduced by nano-sized asperities.

Interplay between stability of aqueous film on nano-rough surface and magnitude of energy barrier in bubble-particle interactions, most likely dictates the rate at which mineral particles are picked up by gas bubbles in flotation systems and can have an important role in flotation kinetics.

CRediT authorship contribution statement

Zhanglei Zhu: Methodology, Validation, Investigation, Writing original draft. Donghui Wang: Resources. Bin Yang: Investigation. Wanzhong Yin: Supervision, Conceptualization. Jaroslaw W. Drelich: Supervision, Conceptualization, Writing - review & editing, Visualization, Project administration.

Declaration of Competing Interest

The authors declare that they have no known competing financial interests or personal relationships that could have appeared to influence the work reported in this paper.

Acknowledgement

The financial supports for this work from the National Natural Science Foundation of China under the grant No. 51874072, the

Fundamental Research Funds for the Central Universities under the grant No. N180106006 are gratefully acknowledged. Zhanglei Zhu also appreciates the China Scholarship Council (No. 201906080099) for financial support of his visiting study to Michigan Technological University, USA.

Financial support for purchasing the atomic force microscope at Michigan Tech through NSF-CS-MRI grant (No. 1725818), used in characterization of mineral surfaces, is also acknowledged.

References

- Ahmed, M.M., 2010. Effect of comminution on particle shape and surface roughness and their relation to flotation process. Int. J. Miner. Process. 94 (3–4), 180–191.
- Chau, T.T., Bruckard, W.J., Koh, P.T.L., Nguyen, A.V., 2009. A review of factors that affect contact angle and implications for flotation practice. Adv Colloid Interface Sci 150 (2), 106–115.
- Chen, H., Tang, T., Zhao, H., Law, K.-Y., Amirfazli, A., 2016. How pinning and contact angle hysteresis govern quasi-static liquid drop transfer. Soft Matter 12 (7), 1998–2008.
- Chen, Y., Xia, W., Xie, G., 2018. Contact angle and induction time of air bubble on flat coal surface of different roughness. Fuel 222, 35–41.
- Crabtree, E., Vincent, J., 1962. Historical outline of major flotation developments. In: Fuerstenau, D.W. (Ed.), Froth Flotation: 50th Anniversary Volume. American Institute of Mining, Metallurgical, and Petrolem Engineerings, New York, NY, USA, pp. 39–54.
- Drelich, J., Chibowski, E., Meng, D.D., Terpilowski, K., 2011. Hydrophilic and superhydrophilic surfaces and materials. Soft Matter 7 (21), 9804–9828.
- Drelich, J., Miller, J.D., Induction time measurements for air bubbles on chalcopyrite, bornite, and gold in seawater, in: Drelich, J. (Ed.), Water in Mineral Processing, Proceedings of the First International Symposium, Seattle, WA, February 19-22, 2012, Published by Society for Mining, Metallurgy, and Exploration, Englewood, CO, USA, 2012, pp. 73–85.
- Drelich, J.W., 2018. A simplified analysis of the effect of nano-asperities on particlebubble interactions. Physicochemical Problems of Mineral Processing 54 (1), 10–18.
- Drelich, J.W., 2019. Contact angles: From past mistakes to new developments through liquid-solid adhesion measurements. Adv. Colloid Interface Sci. 267, 1–14.
- Drelich, J.W., Bowen, P.K., 2015. Hydrophobic nano-asperities in control of energy barrier during particle-surface interactions. Surf. Innovations 3 (3), 164–171.
- Drelich, J.W., Marmur, A., 2018. Meaningful contact angles in flotation systems: critical analysis and recommendations. Surf. Innovations 6 (1–2), 19–30.
- Feng, D., Aldrich, C., 2000. A comparison of the flotation of ore from the Merensky Reef after wet and dry grinding. Int. J. Miner. Process. 60 (2), 115–129.
- Guven, O., Celik, M.S., Drelich, J.W., 2015. Flotation of methylated roughened glass particles and analysis of particle-bubble energy barrier. Miner. Eng. 79, 125–132.
- Hassas, B.V., Caliskan, H., Guven, O., Karakas, F., Cinar, M., Celik, M.S., 2016. Effect of roughness and shape factor on flotation characteristics of glass beads. Colloids Surf., A 492, 88–99.
- Hicyilmaz, C., Ulusoy, U., Bilgen, S., Yekeler, M., 2005. Flotation responses to the morphological properties of particles measured with three-dimensional approach. Int. J. Miner. Process. 75 (3–4), 229–236.
- Jiang, Y., Sun, Y., Drelich, J.W., Choi, C.-H., 2018. Spontaneous spreading of a droplet: The role of solid continuity and advancing contact angle. Langmuir 34 (17), 4945–4951.
- Karakas, F., Hassas, B.V., 2016. Effect of surface roughness on interaction of particles in flotation. Physicochem. Probl. Miner. Process. 52 (1), 18–34.
- Lai, L., Irene, E., 1999. Area evaluation of microscopically rough surfaces. J. Vacuum Sci. Technol. B: Microelectron. Nanometer Struct. Process., Measur., Phenomena 17 (1), 33–39.
- Li, Z., Rao, F., Corona-Arroyo, M.A., Bedolla-Jacuinde, A., Song, S., 2019. Comminution effect on surface roughness and flotation behavior of malachite particles. Miner. Eng. 132, 1–7.
- Qian, J., Gao, H., 2006. Scaling effects of wet adhesion in biological attachment systems. Acta Biomater. 2 (1), 51–58.
- Ramon-Torregrosa, P., Rodríguez-Valverde, M., Amirfazli, A., Cabrerizo-Vílchez, M., 2008. Factors affecting the measurement of roughness factor of surfaces and its implications for wetting studies. Colloids Surf., A 323 (1–3), 83–93.
- Shean, B., Cilliers, J., 2011. A review of froth flotation control. Int. J. Miner. Process. 100 (3–4), 57–71.
- Sun, Y., Jiang, Y., Choi, C.-H., Xie, G., Liu, Q., Drelich, J.W., 2018a. Direct measurements of adhesion forces of water droplets on smooth and patterned polymers. Surf. Innovations 6 (1–2), 93–105.
- Sun, Y., Jiang, Y., Choi, C.-H., Xie, G., Liu, Q., Drelich, J.W., 2018b. The most stable state of a droplet on anisotropic patterns: support for a missing link. Surf. Innovations 6 (3), 133–140.
- Sun, Y., Li, Y., Dong, X., Bu, X., Drelich, J.W., 2020. Spreading and adhesion forces for water droplets on methylated glass surfaces. Colloids Surf., A 591, 124562.
- Ulusoy, U., Yekeler, M., 2005. Correlation of the surface roughness of some industrial minerals with their wettability parameters. Chem. Eng. Process. Process Intensif. 44 (5), 555–563.
- Wang, D., Jiang, Y., Zhu, Z., Yin, W., Asawa, K., Choi, C.-H., Drelich, J.W., 2020. Contact Line and Adhesion Force of Droplets on Concentric Ring-Textured Hydrophobic Surfaces. Langmuir 36 (10), 2622–2628.

- Wenzel, R.N., 1936. Resistance of solid surfaces to wetting by water. Ind. Eng. Chem. 28 (8), 988–994.

 Xia, W., 2017. Role of surface roughness in the attachment time between air bubble and flat ultra-low-ash coal surface. Int. J. Miner. Process. 168, 19–24.
- Xing, Y., Zhang, Y., Liu, M., Xu, M., Guo, F., Han, H., Gao, Z., Gao, Y., Gui, X., 2019.
 Improving the floatability of coal with varying surface roughness through hypobaric
- treatment. Powder Technol. 345, 643-648.
- Treatment. Powder Technol. 343, 043-046.

 Zhu, Z., Wang, D., Yang, B., Yin, W., Ardakani, S., Yao, J.W., Drelich, J., 2020. Effect of nano-sized roughness on the flotation of magnesite particles and particle-bubble interactions. Miner. Eng. 151, 106340.